4D Printed Programmable Shape-Morphing Hydrogels as Intraoperative Self-Folding Nerve Conduits for Sutureless Neurorrhaphy

Akshat Joshi, Saswat Choudhury, Vageesh Singh Baghel, Souvik Ghosh, Sumeet Gupta, Debrupa Lahiri, G. K. Ananthasuresh, and Kaushik Chatterjee*

There are only a few reports of implantable 4D printed biomaterials, most of which exhibit slow deformations rendering them unsuitable for in situ surgical deployment. In this study, a hydrogel system is engineered with defined swelling behaviors, which demonstrated excellent printability in extrusion-based 3D printing and programmed shape deformations post-printing. Shape deformations of the spatially patterned hydrogels with defined infill angles are computationally predicted for a variety of 3D printed structures, which are subsequently validated experimentally. The gels are coated with gelatin-rich nanofibers to augment cell growth. 3D-printed hydrogel sheets with pre-programmed infill patterns rapidly self-rolled into tubes in vivo to serve as nerve-guiding conduits for repairing sciatic nerve defects in a rat model. These 4D-printed hydrogels minimized the complexity of surgeries by tightly clamping the resected ends of the nerves to assist in the healing of peripheral nerve damage, as revealed by histological evaluation and functional assessments for up to 45 days. This work demonstrates that 3D-printed hydrogels can be designed for programmed shape changes by swelling in vivo to yield 4D-printed tissue constructs for the repair of peripheral nerve damage with the potential to be extended in other areas of regenerative medicine.

1. Introduction

4D printing is trending in the rapidly growing field of additive manufacturing with the prospect of impact in several domains, including healthcare.[1,2] This emerging technology enables the fabrication of complex and dynamic structures, which are otherwise difficult to realize using conventional 3D printing.[3,4] 4D printing utilizes either smart materials that respond to specific stimuli,[5,6] programmed design during printing,[7,8] or a combination of both.[9–11] There is a wide range of smart materials that respond to stimuli,[12,13] such as changes in pH,[14,15] temperature,[16] light,[17,18] moisture,[19,20] magnetic field,[21,22] and so on. In recent years, the rapid advancements in tissue engineering combined with an expanded choice of biomaterials have motivated research in 4D printing for regenerative medicine.[23–25] However, the fabrication of complex constructs that faithfully mimic tissue architecture persists as a challenge. Hydrogels are the ideal candidates for engineering tissue scaffolds,[26,27] owing to their biocompatibility, high water-absorption capacity, and chemical tunability. Nevertheless, the choice of hydrogels for 4D printing is rather limited owing to their poor printability and shape fidelity and the limited choice of stimuli that are physiologically relevant while exhibiting good biocompatibility.[28,29] Moreover, controlling the time scale and

A. Joshi, S. Choudhury, K. Chatterjee
Centre for Biosystems Science and Engineering
Indian Institute of Science
Bangalore 560012, India
E-mail: kchatterjee@iisc.ac.in

V. S. Baghel, G. K. Ananthasuresh
Department of Mechanical Engineering
Indian Institute of Science
Bangalore 560012, India

S. Ghosh, D. Lahiri
Biomaterials and Multiscale Mechanics Lab
Department of Metallurgical and Materials Engineering
Indian Institute of Technology Roorkee
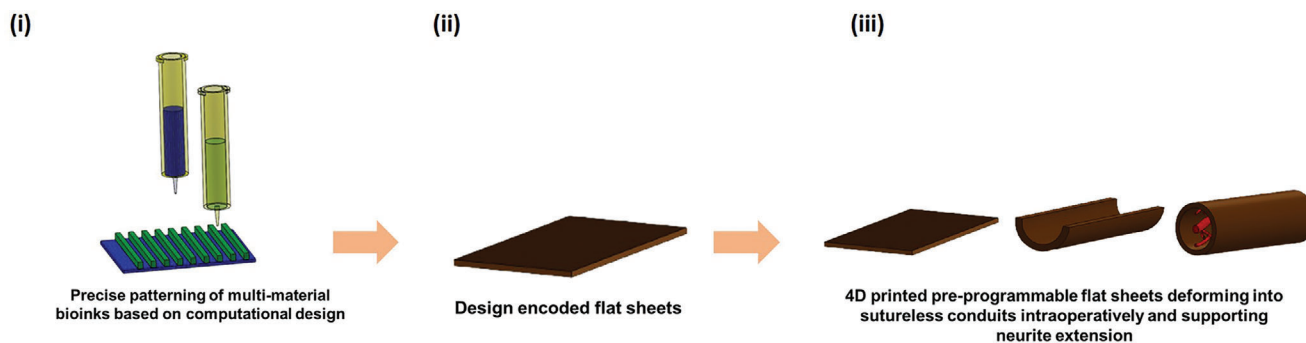Roorkee 247667, India

S. Ghosh
Molecular Endocrinology Lab
Department of Biotechnology
Indian Institute of Technology Roorkee
Roorkee 247667, India

S. Gupta
Department of Pharmacy
Maharshi Markandeshwar University
Mullana 133207, India

K. Chatterjee
Department of Materials Engineering
Indian Institute of Science
Bangalore 560012, India

**ADVANCED
SCIENCE NEWS**

www.advancedsciencenews.com

**ADVANCED
HEALTHCARE
MATERIALS**

www.advhealthmat.de

Scheme 1. Process of fabrication of 4D printed nerve conduits with intraoperative shape deformation capability. i) 3D printing of multi-material bioinks with precise patterning based on computational design. ii) 3D printed design encoded flat hydrogel sheets. iii) Intraoperative deformation of hydrogel sheet into nerve conduits demonstrating capability for neurite extension and nerve regeneration.

tendency of deformation is often challenging, as it necessitates smart design.[30]

A critical limitation of 3D printing is the static nature of the fabricated hydrogels, requiring surgical implantation.[31] This strategy demands inconvenient surgical sutures that are often accompanied by complications, including additional traumatic damage and severe inflammation around the injured tissue.[32] 4D printing offers a promising route to generate dynamic shape-morphing geometries out of static parts while leveraging the benefits of near-near-net-shape manufacturing of complex and patient-specific parts. Target designs are encoded during the printing process, which governs the resulting shape deformations post-printing. Hydrogels can swell in response to water uptake and hence, are the material of choice by researchers developing 4D printed biomaterials. Few recent studies report shape deformations of hydrogels, primarily governed by anisotropic swelling, gradients in cross-linking densities, etc. However, their applications in vivo are limited due to poor control on programming specific shape deformations in constructs prepared from a single material,[28,33] the prolonged time required for the deformations,[29] complex bioink preparation,[34] and poor control on processes to impart anisotropy within the materials.[35–37] These drawbacks hinder the widespread adoption of 4D printed gels for applications necessitating intraoperative shape deformations of deployable devices in minimally-invasive procedures. In vivo 3D printing of scaffolds for tissue regeneration has been demonstrated,[38] but 4D printed hydrogels with in vivo shape-morphing ability are yet to be realized. Among several potential biomedical applications, self-folding nerve conduits that alleviate tedious suturing could benefit the large patient population requiring microsurgeries for nerve repair.[39]

Shape change of 3D printed hydrogels is primarily governed by the material characteristics that induce differential swelling[23,34] and through the programmed design of the printed parts for predetermined controlled deformations.[7,8] Analytical models to predict and elucidate the changes are challenging to formulate, owing to the large and geometrically nonlinear deformations. Computational models have been proposed to semi-quantitatively elucidate the deformations for a designed part.[7]

In this work, we present a dual-component hydrogel system prepared from alginate and methyl cellulose (A/MC), wherein the fractions of the two components were tuned to obtain gels of different swelling ratios. A model was developed to predict shape deformations for parts prepared using these hydrogel formulations. Validation of the model was attempted by correlating the deformations of a wide variety of gel constructs fabricated by extrusion-based 3D printing. The cytocompatibility was assessed, and surface modification by deposition of nanofibers was explored to augment the cellular response to the 4D printed gel. Toward clinical translation of the 4D-printed gel as sutureless nerve guiding conduits (NGCs), the printed gel sheets were implanted to form conduits by in situ shape change in a rat sciatic nerve defect model (**Scheme 1**). Nerve regeneration mediated by the sutureless conduits was assessed up to ≈6 weeks post-implantation. Overall, the study aimed to establish the promise of 4D printed in vivo self-rolling conduits for peripheral nerve regeneration.

2. Results and Discussion

A dual-component hydrogel system was utilized in this work. Two formulations of A/MC were prepared with different fractions of A and MC such that one resulting gel (A/MC: 3/9 by mass prepared in deionized [DI] water) exhibited a higher swelling rate, and the other (A/MC: 4/6 in 5 mM $CaCl_2$ solution) exhibited a relatively lower swelling rate. These compositions were identified after careful evaluation of the printability and swelling rates of several formulations. The physicochemical properties of the individual gels were characterized initially. Morphological analysis by scanning electron microscopy (**Figure 1**a) revealed that the gels were highly porous with interconnected pores. Notably, A/MC:3/9 contained bigger pores than A/MC:4/6, as evident from the cross-sectional SEM micrographs in Figure S2, Supporting Information. This trend corroborates the swelling measurements (Figure 1b), which show that A/MC:3/9 swells considerably more than A/MC:4/6.

Rheological characterization to assess the printability and viscoelastic behavior of the gels confirmed the shear-thinning behavior of both hydrogels (Figure 1c), rendering them suitable for extrusion-based 3D printing.[40,41] Figure 1d reveals the viscoelastic properties of the gels with storage moduli values higher than loss moduli in the entire linear viscoelastic (LVR) region. Figure 1e shows that the gels were thixotropic such that the viscosities of both the gels decrease under high shear rates and consequently recover to the original values upon releasing the stress. This property endows the gels with good printing fidelity and is
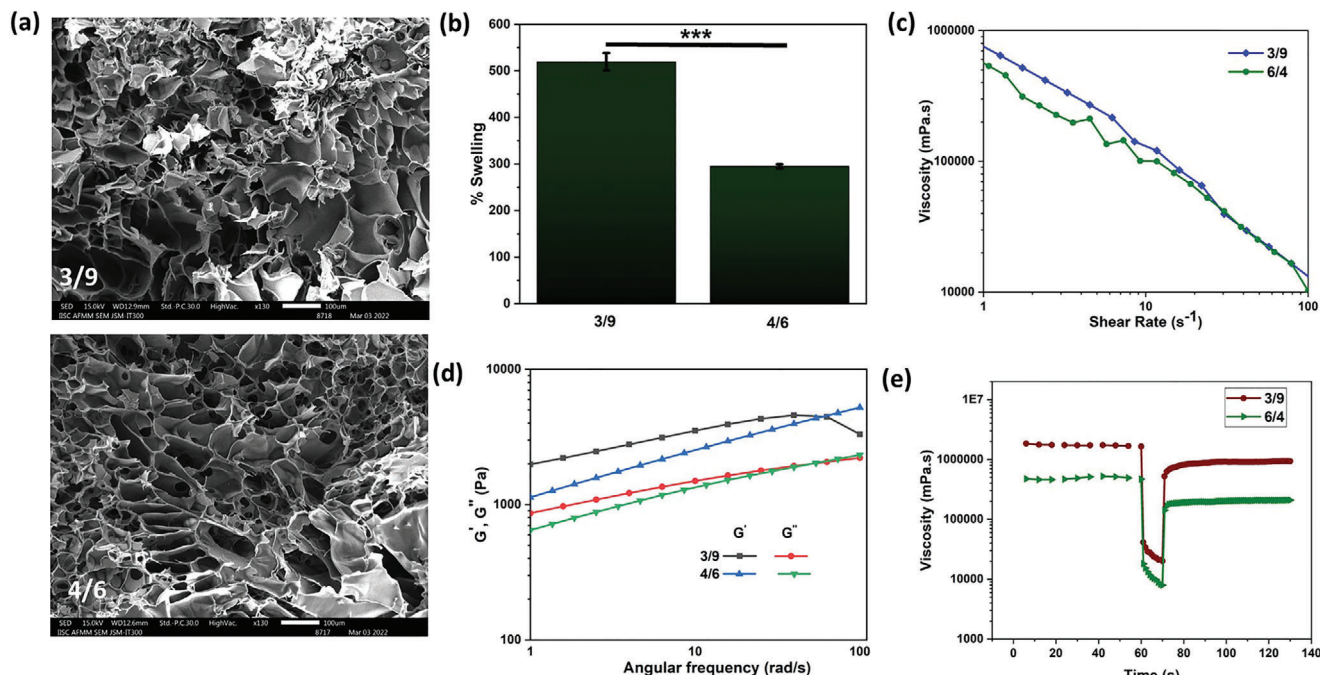
**ADVANCED
SCIENCE NEWS**

www.advancedsciencenews.com

**ADVANCED
HEALTHCARE
MATERIALS**

www.advhealthmat.de

Figure 1. Characterization of the A/MC: 3/9 and 4/6 hydrogels. a) SEM image revealing that both gels are porous (Scale bars are 100 µm); b) Swelling ratios for the two gels; c–e) Rheological analysis of the gels; c) Shear-thinning behavior, d) viscoelastic properties of the two gels, and e) thixotropic properties of the two gels. (*** denotes $p < 0.001$).

a consequence of chain disentanglements and re-entanglements simultaneously under high and low shear rates, respectively.[42,43]

A computational model was formulated to reliably predict the different shape deformations of the 3D printed structures with defined infill patterns. We used a thermal expansion model to simulate the deformations of the hydrogels after establishing a quantitative correlation between the swelling model. The details of the model used are provided in the Supporting Information (Section S1, Supporting Information). We proceeded with modeling the deformations of flat structures with different topographies.

At first, the effect of the topography of the top layer on the shape deformation was evaluated by designing a simple tri-layered trapezoidal geometry. The first layer was a solid base material of higher expansion coefficient, which was decorated with stripes of the second material of lower expansion coefficient placed precisely at different orientations with respect to the base layer (**Figure 2**a[i–iii]). The expansion coefficients for the two materials were calculated from the swelling ratios of the two gels. FEA (finite element analysis) simulations (Figure 2a[iv–vi]) revealed that a trapezoid could deform remarkably differently for the varied arrangements between the two layers, namely, bending along the longer axis for stripes placed parallel (or at 0°) with respect to the long axis of the base layer, twisting for stripes at 45°, and bending along the shorter axis for stripes at 90°. To validate the results determined from the computational model, we designed G-codes to match the computational design (refer to Figure 2b[i–iii]) with details for each layer compiled in Figure S7, Supporting Information. An extrusion-based 3D printer with two nozzles for the two gel formulations was used to print the gels following these G-codes for three different designs. The printed

structures were air-dried for 8–10 h and subsequently swelled in 200 mM CaCl$_2$ solution to initiate the shape deformation. The resultant deformations are compiled in Figure 2b(iv–vi), revealing that the deformations indeed occurred differently and closely matched the computed results. The real-time deformations were recorded (refer to Videos S1–S3, Supporting Information).

To further validate the accuracy of the model in predicting the shape deformations of the 3D printed gels, we designed a variety of complex geometries with varied infill patterns (G-codes shown in Figure S8, Supporting Information). A cross (or plus cross) construct was designed such that the stripes of the top layer were placed at different angles with respect to the base layer, as shown in **Figure 3**a(i,ii). As seen from simulations, the cross geometry can be predetermined to bend or twist by varying the arrangement of the stripes (Figure 3a[iii,iv]). Gels were 3D printed with corresponding G-codes (Figure 3b[v,vi]). When the dried gels were allowed to swell in CaCl$_2$ solution, observed deformations closely matched the deformations determined computationally (refer to Figure 3b[vii,viii] and Videos S4 and S5, Supporting Information). We demonstrated different predetermined modes of deformation in petals governed by defined infill patterns (refer to Figure 3c[i,ii] computational design, [iii,iv] simulated deformation; Figure 3b[v,vi] corresponding G-codes, [vii,viii] corresponding experimental deformation and Videos S6 and S7, Supporting Information). Finally, we investigated the deformation of gels prepared in the shapes of a butterfly and a rectangle (refer to Figure 3e,f and Videos S8 and S9, Supporting Information for the butterfly geometry and Figure 3g,h and Videos S10 and S11, Supporting Information for the rectangular geometry). Toward enhancing the attachment and growth of cells on the gel surface, the dried gel was coated by airbrushing a thin layer of nanofibers
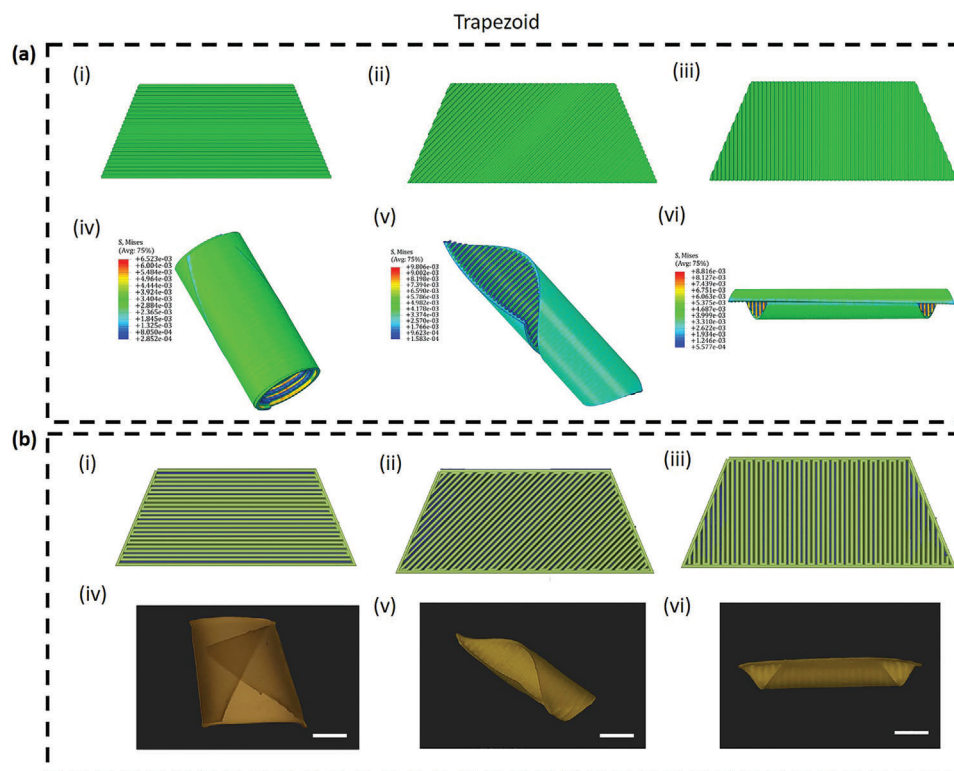
Figure 2. FEA simulations and experimental validation of shape deformations. a) Computational analysis wherein (i–iii) are the modeled geometries and (iv–vi) are the corresponding simulated deformations. b) Experimental validation wherein (i–iii) are the modeled G-codes and (iv–vi) represent the digital photographs of the deformed gels. Scale bars: 12 mm.

prepared by blending gelatin and polycaprolactone (PCL). It is to be noted here that the time and tendency of shape deformations were not impacted by nanofiber deposition, as demonstrated in Supporting Information (Section S2, Supporting Information).

We confirmed that our hydrogels (both uncoated and nanofiber-coated gels, hereafter termed uncoated and coated, respectively) were biocompatible in vitro and in vivo (Section S2, Supporting Information) and that nanofibers do not impact shape deformation (Section S2, Supporting Information). Next, we aimed to demonstrate the clinical benefit of the shape-changing 4D printed hydrogel focusing on its utility as sutureless NGCs. Toward this goal, rectangular models were designed for fabrication by 3D printing to self-roll into tubular constructs of predetermined dimensions upon stimulation with CaCl$_2$ solution. Digital photographs of the tubular construct post-deformation and its SEM image are compiled in Figure S9, Supporting Information. Mechanical testing of the 4D-printed nerve conduit was performed to assess the stability and durability under cyclic loading. The stress response of the conduits was marked by hysteresis for the first cycle (Figure S9, Supporting Information) but not in the subsequent nine cycles of loading and unloading, indicating good recovery of the stresses upon unloading with minimal energy losses. Thus, the self-rolled gel matches the biomechanics of soft tissues and is well-suited for engineering NGCs.

Several artificial conduits for nerve regeneration have been developed, some of which have been approved for clinical use by the Food and Drug Administration (FDA).[44] In both preclin-ical and clinical trials, the single tubular structure, NeuraGen and Neurolac, derived from type I collagen and PCL, respectively, showed promising outcomes.[45] However, both of these commercially-available conduits require suturing. Even though sutures are widely accepted as the standard therapy for peripheral nerve injury (PNI), they are not without risk, including further traumatic injury and severe inflammation surrounding the wounded nerve tissues, preventing effective regeneration of the nerve.[46] Hence, in an attempt to establish a rapid and efficient neurorrhaphy treatment for improving prognosis without any severe inflammatory complications, the 4D printed conduit designed in this study was assessed for potential sutureless neurorrhaphy in PNI treatment.

Owing to its biocompatibility, biomechanical properties, and rapid self-rolling ability upon stimulation, we posited that the 4D-printed rectangular gel sheets could be placed at the injury site to self-roll into a conduit in vivo for covering the severed ends of the resected nerve. Such an intraoperative 4D-printed device could offer a marked advantage over the current technology by reducing the complexity and duration of surgeries to facilitate axonal growth and eventual regeneration and restoration of nerve function. The efficacy of 3D-printed gel sheets (with and without the nanofiber coating) as intraoperative deployable implanted nerve conduits was assessed in a well-established 2 mm sciatic nerve defect model in Sprague–Dawley rats and evaluated for up to 6 weeks (**Figure 4**a). The animals were randomly segregated into four different groups, namely, sham, negative, and uncoated and coated 4D printed gels. No surgical damage was done to the
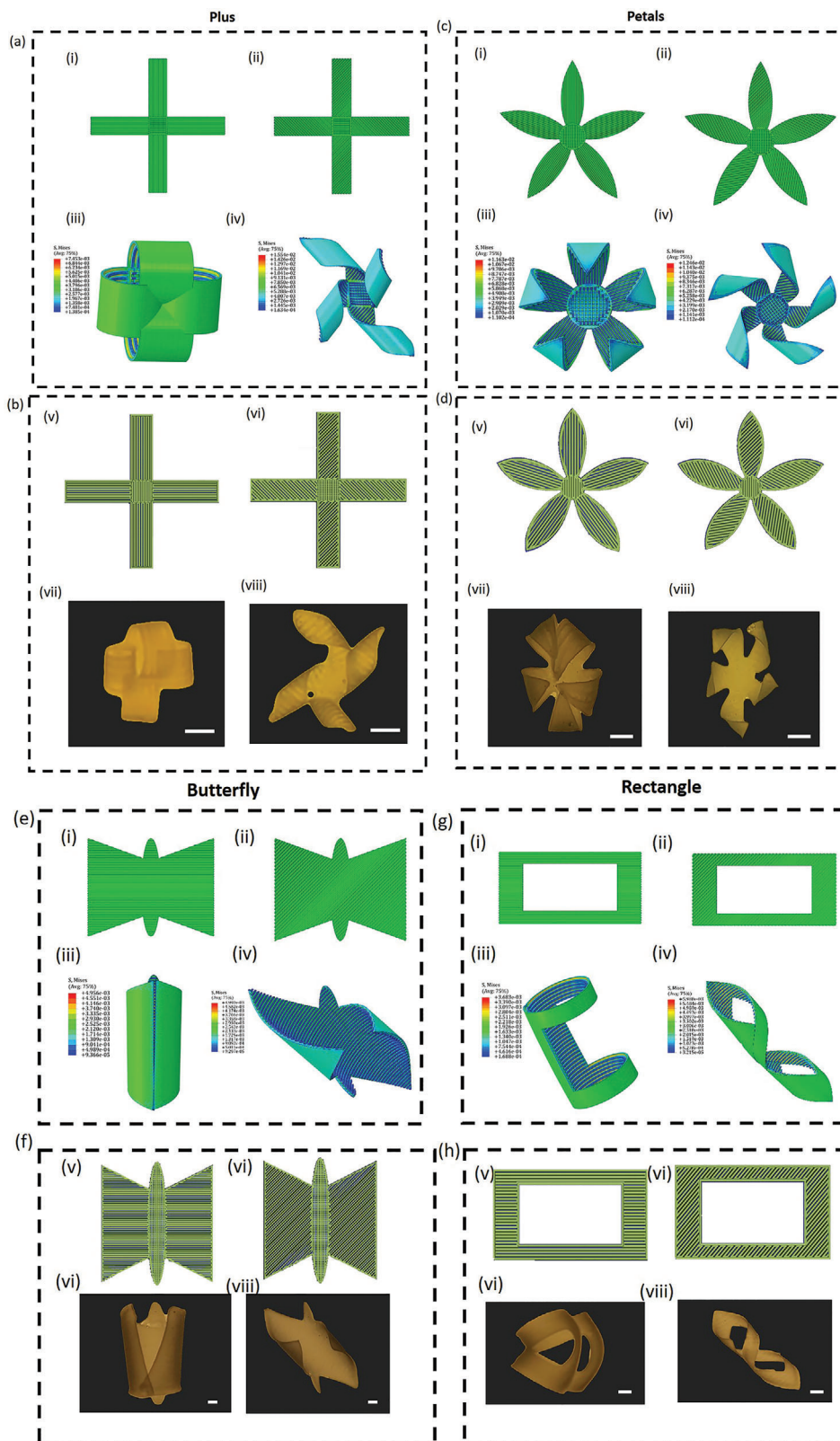
ADVANCED
SCIENCE NEWS

www.advancedsciencenews.com

ADVANCED
HEALTHCARE
MATERIALS

www.advhealthmat.de

Figure 3. FEA simulations and corresponding experimental validation for different geometries. a) Computational evaluation for a cross-shaped geometry; i,ii) Design showing different stripe angles, and iii,iv) Effect of stripe angle on corresponding deformations determined computationally. b) Experimental validation; v,vi) The G-codes created based on computational designs, and vii,viii) The resultant deformations validated experimentally. c) Computational evaluation for a petal-shaped geometry; i,ii) Design showing different stripe angles and iii,iv) effect of stripe angle on the corresponding

ADVANCED
SCIENCE NEWS
www.advancedsciencenews.com

ADVANCED
HEALTHCARE
MATERIALS
www.advhealthmat.de

animals in the sham group. Self-healing damage served as the negative control. The procedure of wound infliction and the in vivo shape deformation are presented in Figure S10, Supporting Information. The hydrogel-wrapped regions of the transected sciatic nerves 6 weeks post-surgery are shown in Figure 4b. No animals were lost during the test period. A combination of functional and structural assessments was analyzed to determine the success of nerve regeneration. Functional assessments such as the sciatic function index (SFI), hot plate latency, and paw withdrawal threshold were performed at specific intervals for 6 weeks, following which rats were sacrificed to assess the restoration of motor function in the wound-inflicted leg.

SFI measures the level of activity in the sciatic nerve. SFI was calculated by comparing the geometric representation of the damaged hind paw of an injured rat and the representation of the contralateral paw. Herein, the paw prints of the operated legs and their corresponding contralateral paws of the animals from all the groups were taken on the 1st, 15th, 30th, and 45th days (compiled in Figure 4c). In contrast to the negative control group, both the conduit-treated groups showed significant increments in SFI measurements 15th day onward post-surgery (Figure 4d). The best SFI values for both the conduit groups were observed on day 45. But among the two groups, the coated group showed a significantly increased SFI, demonstrating the superiority of coated nanofibers. (Figure 4d).

Atrophy of the gastrocnemius muscle (GA) is a common side effect of sciatic nerve damage.[47] Muscle atrophy is reduced by the regeneration of the sciatic nerve and reinnervation of the GA. GA weight analysis was used to evaluate muscle atrophy and regeneration. After the animals were sacrificed, the gastrocnemius muscles of both hind legs were removed and weighed. The left (L) (muscle weight of operated left leg)/ right (R) (muscle weight of normal right leg) ratio was determined for all the groups (Figure 4e). After weighing, the lowest L/R ratio was observed for the negative group, whereas it was markedly improved in the case of conduit-treated groups. No significant difference in the L/R ratio was observed among the two conduit groups (Figure 4e). This observation was corroborated by the digital photographs of the gastrocnemius muscles (Figure S11, Supporting Information). Muscle atrophy and regeneration assessed by hematoxylin and eosin (H&E) staining of the GA muscle (Figure 4f) indicated that the mass, integrity, and morphology of the muscle were considerably lost in the negative group (Figures 4f-ii,g). These parameters were markedly improved in animals treated with the 4D printed conduits following the sciatic nerve injury (Figures 4f [iii,iv], g), which were comparable to the sham group. Thus, both conduits (coated and uncoated) repaired the sciatic nerve, reinnervating the gastrocnemius muscle and reducing muscular atrophy as a result of regeneration.

The hot plate and Randall–Selitto tests were used to assess the efficacy of conduits in restoring functional motor activity. In the hot plate study, the amount of time that each animal was able to withstand the heat or wait before displaying a reaction was recorded. When the sciatic nerves of the animals are compromised, the animals have longer latency durations. This period proportionally decreases as the sciatic nerve regenerates. Figure 4h reveals that the maximum latency period was observed in the negative groups during the post-operative six weeks. The heat latency period was significantly reduced in the 4D printed conduit-treated groups, with maximum improvements observed on day 45. On the 45th day, the heat latency period for the uncoated and coated conduits was ≈13 and ≈11 s, respectively, which were significantly lower than the negative group (≈24 s) (Figure 4h). Moreover, animals in the coated conduit group showed a statistically significant reduction in the heat latency period compared to animals in the uncoated group (Figure 4h). The Randall–Selitto (Paw withdrawal threshold) test determines allodynia or neuropathic pain in the animals. Allodynia, a hypersensitivity to a pain signal, is induced by nerve damage as a result of trauma or illness.[48] Weights provide quantifiable pressure on the injured leg in the experimental and sham-operated groups. The paw withdrawal threshold is a measure of the pressure at which an animal withdraws its paw (PWT). Figure 4i reveals that pain hypersensitivity was more successfully suppressed when the damaged sciatic nerves were treated with coated or uncoated conduits. The PWT for uncoated and coated conduits were ≈15 and ≈16 g, respectively, on day 45 post-injury. The PWT for the negative group was ≈6 g. The 135% and 150% improvement observed in the uncoated and coated conduits, respectively, compared to the negative group, demonstrates the functional recovery of the resected sciatic nerve with the 4D printed nerve conduit deployed intraoperatively. However, no significant difference in PWT was observed between the uncoated and coated groups.

The low levels of the biochemical marker, immunoglobulin IgE, eliminated adverse immunogenic responses induced by the implanted conduit (Table S3, Supporting Information). Histological analysis of organs, including the liver and the kidney, further confirmed the cytocompatibility of the implanted hydrogel (Figure S12, Supporting Information).

Histological investigation of the different groups revealed the success of nerve tissue regeneration. Regenerated nerve tissue was observed in the longitudinal slices of samples stained with H&E six weeks post-surgery (**Figure 5**a,b). Here, the staining of the negative control group is excluded, as no nerve connection was established between the two resected ends. H&E staining of the cross sections (Figure 5a[i-vi]) and longitudinal sections (Figure 5A[vii-ix]) in the middle of the region covered by the conduit shows that nerves and Schwann cells (SCs) were developing into the transplanted conduit, demonstrating that the injured nerves were being regenerated at the proximal end. Quantification of the H&E-stained positive area of the nerve from uncoated (Figures 5a[ii,v,viii],b) and coated conduit groups (Figure 5a[iii,vi,ix],b) confirmed more regenerating nerve fibers in the coated conduit group than in the uncoated group.

---

deformations determined computationally. d) Experimental validation; v,vi) The G-codes created based on computational designs, and vii,viii) The resultant deformations validated experimentally. e) Computational evaluation for a butterfly-shaped geometry. i—iv) Stripes placed at different angles can control the wing movement. f) (i–viii) Corresponding G-codes and deformed outcomes of the butterfly wing movement. g) Rectangle-shaped geometry can be designed to deform into complex geometries by varying the arrangement of stripes; i–iv) Computational design and deformations. h) Deformed gel of rectangular shape geometry; v–viii) G-codes and corresponding to deformations observed experimentally. Scale bars: 5 mm.
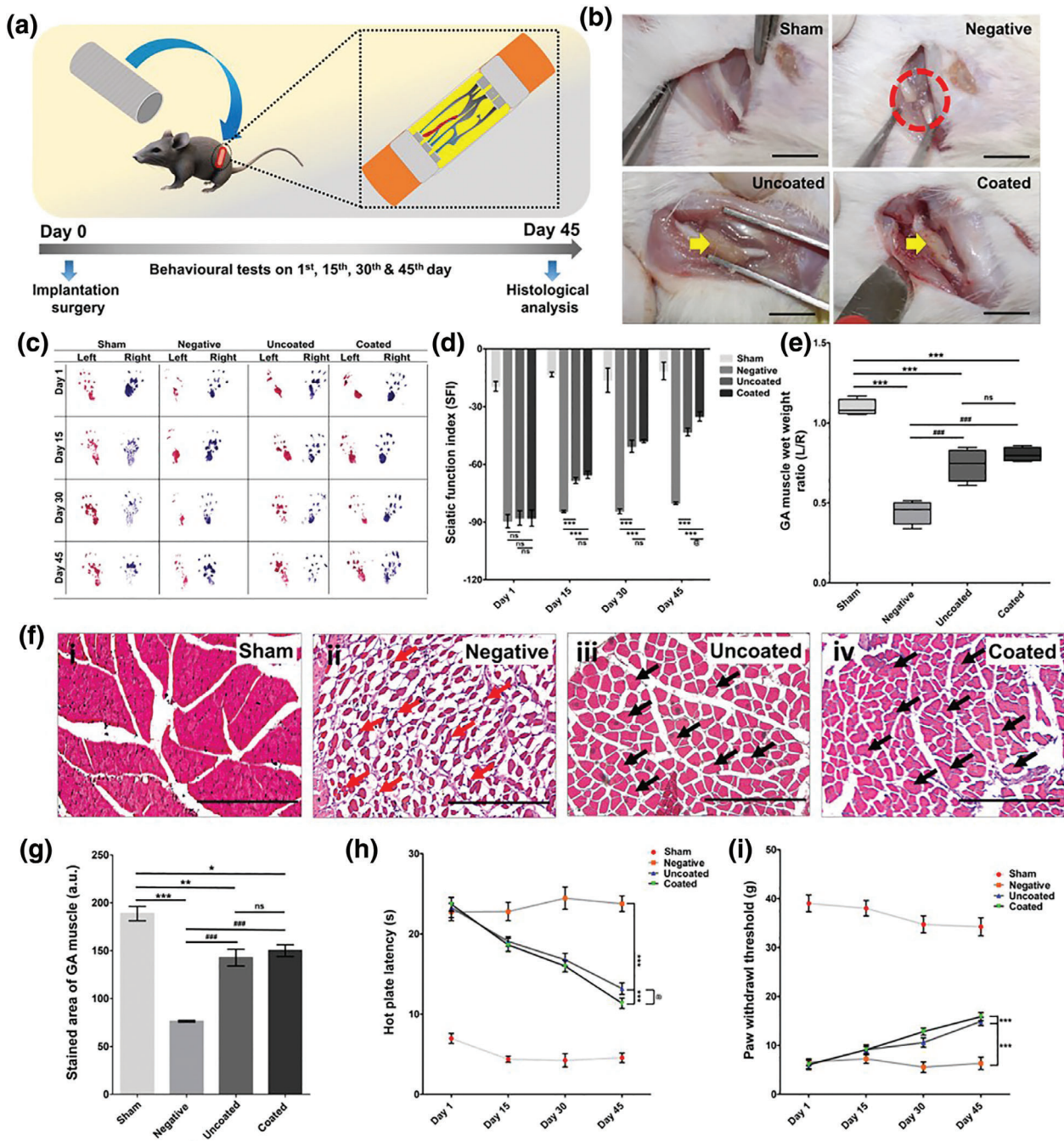
Figure 4. Direct and indirect functional assays to assess the regeneration capability of the scaffolds. a) Schematic diagram of implanting scaffolds into sciatic nerve transected SD rat model. b) Digital images of scaffold implantation site taken on 45th day after the surgery in different groups (Scale bar: 1 cm). Yellow arrow indicates the area of wrapped scaffolds. Red dotted circle indicates the non-regenerated damaged nerve in the negative group. c) Digital images of the footprints of the left and right hind foot. Individual photos of left and right paw prints of animals from different groups at each time point were assembled to create the image. Red-colored paw print: Left hind leg; Blue-coloured paw print: Right hind leg. d) Quantitative estimation of SFI of different groups at each time point. (*** denotes $p < 0.001$ vs negative; @ denotes $p < 0.05$ vs uncoated). e) Measurements of the gastrocnemius muscle (GA) wet weight ratio (left/right). (*** denotes $p < 0.001$ vs sham; ### denotes $p < 0.001$ vs negative). f) (i–iv) H&E-stained images of the GA muscle of the left hind leg (operated limb) of rats from different experimental and sham groups. (Scale bar: 200 µm). The degenerated muscle fibrils (in the negative group) and the regenerated muscle fibrils (Uncoated and coated groups) have now been indicated with red and black arrows respectively. g) Quantification of H&E-stained area of the GA muscle. Data are presented as mean ± SD. ($n = 4$). (*, **, and *** represent $p < 0.05$, $p < 0.01$, and $p < 0.001$, respectively vs sham; ### denotes $p < 0.001$ vs negative). h) Graph representing the hot plate latency periods of the animal from different groups. Data are presented as mean ± SD. ($n = 4$). (*** denotes $p < 0.001$ vs negative; @ denotes $p < 0.05$ vs uncoated) i) Graph representing the paw withdrawal threshold (PWT) of the animal from different groups. Data are presented as mean ± SD. ($n = 4$). (*** denotes $p < 0.001$ vs negative). (ns: non-significant).

**ADVANCED
SCIENCE NEWS**

www.advancedsciencenews.com

**ADVANCED
HEALTHCARE
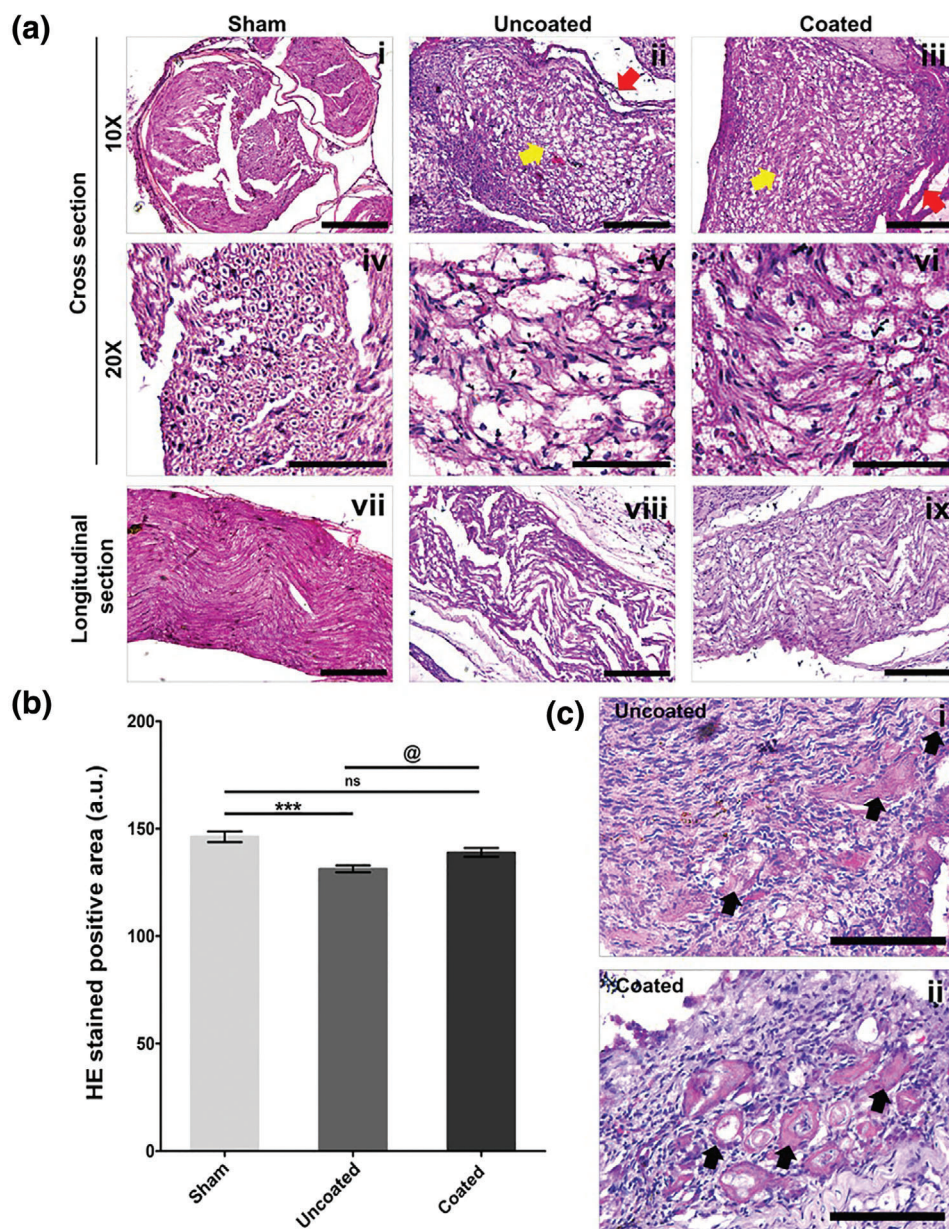MATERIALS**

www.advhealthmat.de

Figure 5. Assessment of the nerve regeneration potential of conduits (coated and uncoated) through histological analysis. a) Bright-field pictures of H&E-stained transverse slices of sciatic nerves of rats belonging to various groups: i,iv,vii) sham, ii,v,viii) uncoated, and iii,vi,ix) coated group. Scale bar for (i–iii) and (vii–ix): 200 μm; Scale bar for (iv–vi): 50 μm. Yellow arrows indicate the regenerated nerve area; red arrows indicate the remnant scaffolds. b) Quantification of H&E stained positive area. Data are presented as mean ± SD. (*n* = 4). (*** denotes *p* < 0.001 vs sham; @ denotes *p* < 0.05 vs uncoated). c) H&E-stained sections of the remnant of the wrapped scaffolds in the nerve injury area. Black arrows indicated the blood vessels. Scale bar: 50 μm.

The integrity of the regenerated nerve was also better in the coated group (Figure 5a[iii,vi,ix]) compared to the uncoated (Figure 5a[ii,v,viii]) groups. This enhancement in the coated group was possibly due to the biocompatible fibrous coating in the lumen of the formed tube, which mimics the natural extracellular matrix of the tissue. This fibrous coating provided the ideal environment for the Schwann cells to grow on the fibers to utilize them as tracks on which the axon could be regenerated. The findings of the H&E staining demonstrated that the

sham-operated group had intact nerve fibers (Figure 5a[i,iv,vii]). These results confirm that the surface topography of tissue scaffolds played a critical and essential role in guiding the reconstruction of nerves. Furthermore, Figure 5c(i,ii) indicates that blood vessels were formed in both conduits. Blood vessels provide material exchange and enable nourishment to regenerated nerve tissues and SCs, which are essential components for nerve regeneration.[49–52] Therefore, both coated and uncoated gels can aid in the healing of damaged peripheral nerves, as they promote
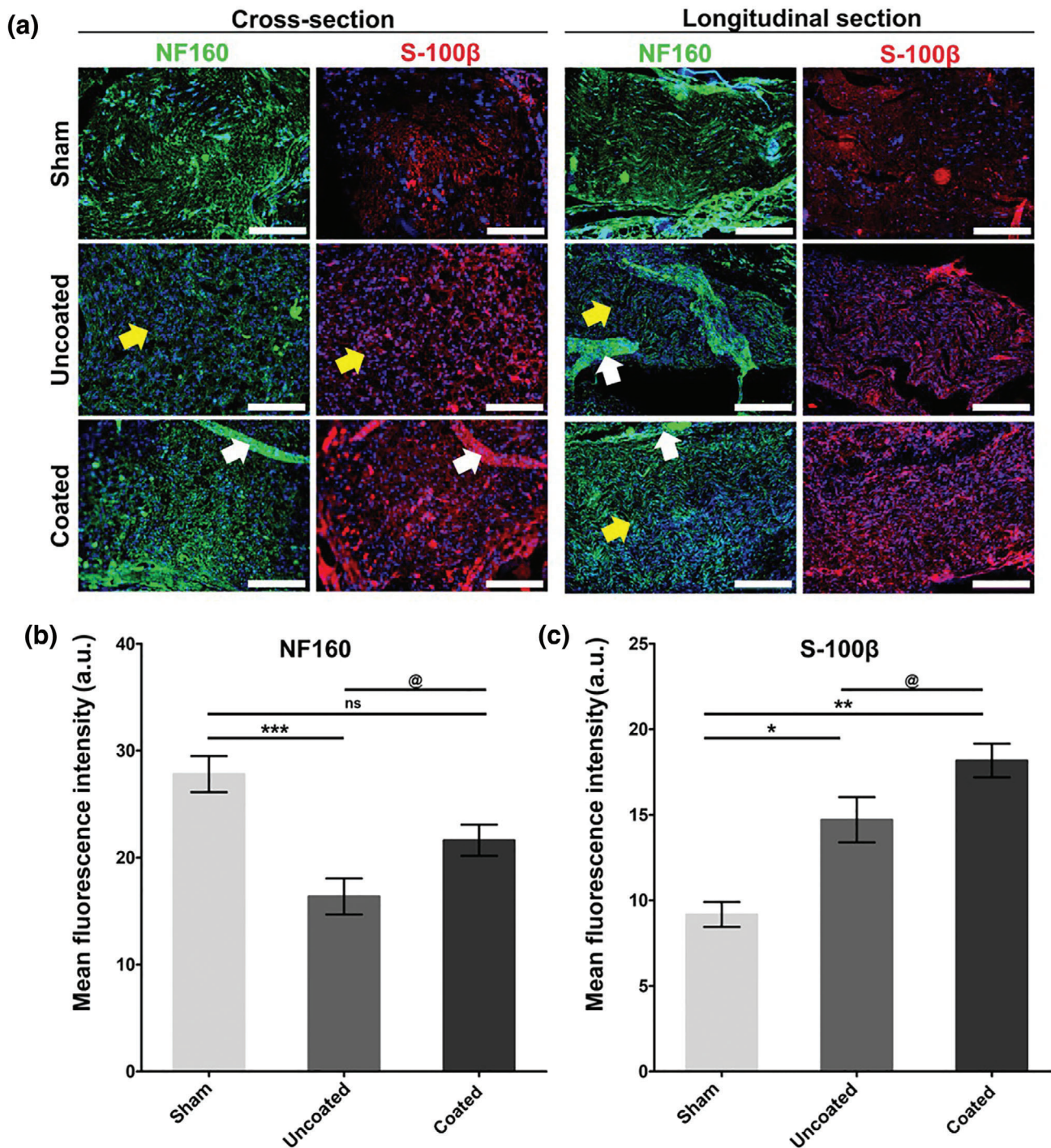
**ADVANCED
SCIENCE NEWS**

www.advancedsciencenews.com

**ADVANCED
HEALTHCARE
MATERIALS**

www.advhealthmat.de

Figure 6. Assessment of the nerve regeneration potential of 4D printed conduits through histology. a) Cross-section and longitudinal sections of sciatic nerves were stained for NF-160 (green) (a marker for neurofilaments), S-100β (red) (Schwann cell marker), and nuclei (blue). Scale bar (cross-sections): 100 µm; Scale bar (longitudinal sections): 200 µm. Yellow arrows indicate the regenerated nerve area; white arrows indicate the remnant scaffolds. Plots of fluorescence intensity for b) NF-160 (*** denotes $p < 0.001$ vs sham; @ denotes $p < 0.05$ vs uncoated) and c) S-100β (* and ** denotes $p < 0.05$ and $p < 0.01$ respectively vs sham; @ denotes $p < 0.05$ vs uncoated). Data are presented as mean ± SD. ($n = 4$).

**ADVANCED
SCIENCE NEWS**

www.advancedsciencenews.com

**ADVANCED
HEALTHCARE
MATERIALS**

www.advhealthmat.de

neovascularization. Nevertheless, further research is warranted to elucidate the underlying mechanisms.

Damage to a peripheral nerve initiates a complex chain of molecular events leading to nerve regeneration. These events include Wallerian degeneration, the axonal response for phagocytosis, chromatolysis, Schwann cell proliferation, axonal growth, and target reinnervation.[53] NF160 (Neurofilament 160), a marker for neurofilaments, is typically seen in cells or tissues of neuronal origin. Axonal regeneration requires the presence of SCs. S100β (S100 calcium-binding protein B) is a characteristic marker for SCs. Thus, both the crosssections and the longitudinal sections of the tissues were immunostained for NF-160 (green) and S100β (red), and the nuclei were counterstained with DAPI (**Figure 6**a). NF-160 and S-100β proteins were expressed in all the study groups, confirming the formation of myelin sheaths composed of SCs and the ingrowth of new axons in the 4D printed conduit. The mean fluorescence intensities of both NF-160 and S-100β were calculated by image processing. The highest NF-160 expression was observed in the sham group containing intact nerve fibers. Notably, the expression of NF-160 was higher in the nanofiber-coated conduits than in the uncoated conduits (Figures 6a [green panels] and 6b). For S-100β, the sham group showed the least expression as no regeneration occurred, whereas the uncoated and coated conduits showed increased S-100β expression due to tissue regeneration (Figures 6a [red panels] and 6c). Notably, the coated group exhibited more expression of S-100β as compared to the uncoated conduit group. Thus, the nanofibrous coating augmented the efficacy of the 4D-printed nerve conduit.

Taken together, the programmable shape-changing hydrogel developed in this work was effective as a 4D-printed NGC. The internal nanofibrous structure further enhanced the conduit performance by altering the gel architecture at both the macroscale and the nanoscale.[54] The presence of gelatin in the nanofibers augments cellular interactions, as observed in vitro, and could enable the attachment of SCs to the conduit.[55] Nanofibers mimic the architectures of extracellular matrices to effectively direct cell fates and functions. Therefore, this fiber-coated gel has the potential to enhance the healing capacity of large-scale lesions in thick nerves.

In a few recent studies, 4D printing has been explored for a few biomaterials, such as silk fibroin methacrylate (SF-MA) and oxidized and methacrylated alginate (OMA). Some of these describe the applicability of the 4D-printed gels in vivo. SF-MA was bioprinted into biomimetic trachea-like structures to heal damaged trachea in rabbits.[23] However, the utility of these systems is limited by extremely slow shape deformations (the time required was up to 1 h) and poor control of the deformations. Moreover, only one type of bending was observed in a given structure. In stark contrast, we demonstrate the ability to realize several deformations in a single structure by varying infill angles, which can yield a wide range of customized tissue-like structures. Moreover, the shape deformations are much faster in our gels (time scales of a few seconds) which is a vital consideration for intraoperative deployment. Ding et al. 4D printed jammed microflake hydrogels (MFH) into cartilage constructs.[34] However, the synthesis of bioinks is complex and is accompanied by prolonged shape deformations ($\approx$2 h) and the absence of in vivo demonstrations. In particular, cellulose-based bioinks have been recently explored

for 3D/4D printing due to their highly thixotropic properties and ease of synthesis.[28] For instance, A/MC gels were shown to exhibit shape changes by varying infill angles,[8] however, the system being a single component was not very structurally stable. Moreover, there was no biocompatibility study to support any tissue function, the shape changes were not predicted by any computational model. The multi-component gel system fabricated in this study exhibited differential swelling in addition to design encoded printing paths, which makes the shape changes predictive through modeling, and the resultant structures are robust. Additionally, the gels were surface-modified with nanofibers to make them conducive for cells.

We focused on demonstrating the utility of the 4D-printed multi-component gels for engineering NGCs, which are primarily used to bridge the gap of a severed nerve while guiding the axons to grow and avoiding scar tissue formation.[56] So far, most research has focused on 3D-printed gels, such as gelatin methacryloyl (GelMA),[57] GelMA/PEGDA,[58] and so on., for preparing NGCs. However, 3D-printed NGCs need suturing with the two nerve ends to secure the NGC at the damaged site, which requires highly skilled surgical techniques. The 4D printed NGCs developed here can be placed intraoperatively over the resected nerve ends to self-roll in vivo, thereby avoiding the need for suturing. This offers a marked potential clinical advancement over the current techniques. 4D printing can be leveraged to personalize the NGC to customize the diameters and lengths to match patient needs and incorporate complex design features such as branching, which would be otherwise difficult to realize.

3. Conclusion

This study presents 4D printable hydrogels that can be programmed to undergo predetermined shape changes in vivo after 3D printing for the repair and regeneration of tissues. Dual-component A/MC hydrogels with varied A/MC ratios were 3D printed along different layers with defined infill patterns to spontaneously change their original as-printed shapes when stimulated by water uptake. The shape changes initially computed from FEA simulations were validated experimentally to generate a variety of complex geometries. The gels were coated with gelatin-rich nanofibers for enhanced cell adhesion. 4D printed tubular geometries were obtained by controlled shape deformations in vivo of the 3D printed gels to serve as intraoperative self-folding NGCs. The 4D-printed conduits clamped the ends of a resected sciatic nerve in a rat model, eliminating the need for suturing. A combination of histological and functional assays established the capability of the 4D-printed conduits for regenerating peripheral nerves following injury. Overall, this study demonstrates the potential of 4D-printed tissue constructs for the repair and regeneration of peripheral nerves and underscores the promise of 4D printing for other applications in regenerative medicine.

4. Experimental Section

Gel Preparation: The hydrogels were prepared as reported previously with modifications.[59] Briefly, for preparing the Alg/MC:3/9 hydrogels, 3% (w/v) alginic acid sodium (Alg; Sigma Aldrich) was added to 4 ml of deionized (DI) water with constant stirring at 60 °C to obtain a clear solution.

Next, 9% (w/v) MC (Viscosity 4000 cP; Sigma Aldrich) was added slowly with continuous stirring at 60 °C until MC dissolved completely, and a homogenous solution was obtained. The resulting solution was then filled in a cartridge used for 3D printing and was kept at 4 °C for 30 min for complete hydration of MC, following which the cartridge was stored at room temperature (RT, ≈25 °C) until further use. For preparing the Alg/MC:4/6 gels, a similar procedure was adopted with 5 mm $CaCl_2$ solution as the medium.

Gel Characterization: The pore morphology of both the gels (Alg/MC:3/9 and Alg/MC:4/6) was characterized using a scanning electron microscope (SEM, JEOL iT 300). The gels were lyophilized and sputter-coated with gold before observation. Swelling studies were performed after drying the gels overnight. The initial dry weight (W_0) of the gels was measured and then soaked in 200 mm $CaCl_2$ solution. The weight (W_t) of the gels was monitored at regular intervals. The extent of swelling was calculated using the equation.

$$\text{Swelling} (\%) = \frac{W_t - W_0}{W_t} \times 100 \tag{1}$$

The viscoelasticity of the gels was characterized using a rotational rheometer (Anton Paar Modular Compact Rheometer- 302) with a 10 mm parallel plate and a 1 mm gap. For the viscosity flow test, the viscosity of the gels was measured at shear rates ranging from 1 to 100 s^{-1}. For the angular frequency sweep, a constant strain of 1% was chosen from the linear viscoelastic region (LVR), and angular frequency was varied from 1 to 100 rad s^{-1}. Thixotropy characterization was performed in three steps: a low shear rate of 0.1 s^{-1} was applied to the gels for 60 s, the shear rate was increased to 100 s^{-1} for 10 s, and finally, the shear rate was lowered to 0.1 s^{-1} for 60 s.

Finite Element Analysis (FEA) Theory and Simulations: Different 3D models were prepared in Solidworks (Dassault Systems), which were then imported into the commercially available FEA software package Abaqus 2017 (Simulia 2017) to predict the deformation of the hydrogel designs experimentally.

4D Printing of Multi-Component Hydrogels: To enable the process of 4D printing, the 3D models were designed in Solidworks (Dassault System), which were converted to StereoLithography (.Stl) format for slicing to generate G-codes (Repetier Host, Cellink). For creating the G-codes, the print paths were defined as per computational designs, wherein a first solid layer of Alg/MC:3/9 was overlaid by stripes of Alg/MC-4/6 placed at different angles on the second and third layers with respect to the first layer. For creating stripes, 40% aligned rectilinear infill patterns with defined fill angles were used, as per computational design. The resulting G-codes were then input to an extrusion-based 3D bioprinter (BioX, Cellink) for 3D printing of the gels independently from two nozzles. The printed constructs were air-dried for 8 h at RT and immersed in 200 mm $CaCl_2$ solution. The resulting shape changes were recorded digitally.

In Vivo Studies on Sciatic Nerve Transected Model: All the animal studies were performed in accordance with 86/609/EEC Act with approvals (numbers MMCP-IAEC-120 and MMCP-IAEC-121) from the Institute Animal Ethical Committee of Maharshi Markandeshwar University, Mullana, following globally-accepted norms (NIH Publications no. 8023, revised 1978). Specifically, adult Sprague-Dawley male rats (between 250–270 grams at the time of surgery) were selected to estimate the efficacy of fabricated scaffolds in the regeneration of PNS involving the earlier described sciatic nerve injury model, as described earlier.[60] A total of 16 animals were arbitrarily divided into four groups – sham-operated (operational control), negative control (injury without any treatment given), uncoated (4D printed rectangular sheets without any fibers coating), and coated (4D printed rectangular sheets with fibers coating). The resulting dimensions of the self-folding sheets were calculated using simulations to yield conduits to sufficiently cover the defect. Each group contained four animals. Sciatic nerve regeneration was investigated in this work using an injury model with a 2 mm transection. Both the coated and uncoated sheets were sterilized through UV irradiation. Before transplantation, the sheets, including coated and uncoated, were stimulated with 200 mm of $CaCl_2$ solution and placed at the defect site. Thereafter, 5 mm
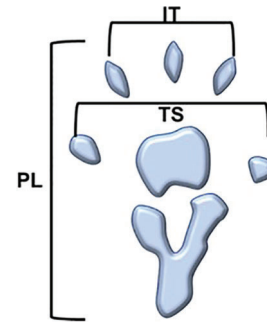
Scheme 2. Schematic diagram of paw indicating the PL, TS, and IT.

$CaCl_2$ was poured over the sheets to induce self-folding into tubular structures spontaneously around the injured nerve due to the pre-programmed deformation. Intraperitoneal injections of ketamine (90 mg kg^{-1}) and xylazine (10 mg kg^{-1}) were used to anesthetize the animals, followed by a bilateral incision at the left lateral thigh. The sciatic nerve was uncovered by cutting through the bicep femoris and gluteus superficial muscles. Each rat had a 2 mm nerve deficit, which was then bridged utilizing different neural scaffolds. Nerve conduits were used to connect the proximal and distal ends of the damaged nerve. As the conduits were wrapped automatically around the wound, thus no suturing was required. A 2-mm segment of the sciatic nerve was removed, and the two ends were left untreated for the negative group. The muscle and skin layers were appropriately sutured with 30 nylon sutures after the implant site had been cleaned and disinfected. To avoid infection, each rat was administered 800 000 units of penicillin immediately following surgery.

Functional Recovery Tests: The functional recovery of the animals was assessed at the 1st, 15th, 30th, and 45th days post-operatively using the hot plate test and Randall-Selitto test to assess thermal reactivity and mechanical threshold, respectively. For thermal reactivity assessment, each rat was individually placed on a metal hot plate of 30 × 30 cm held at 45 ± 1 °C. The frequency with which the left paw was lifted in order to balance the weight on the right paw, which was not damaged, was carefully observed as a reaction to thermal allodynia. The lifting of paws as a result of regular movement was disregarded.[60]

The Randall–Selitto paw pressure test was performed using an analgesy meter. Increasing mechanical pressure was administered to the experimental rat leg on the medical section of the plantar surface of the left hind paws as late as observing a withdrawal response. For each animal, the amount of pressure that caused a withdrawal reaction was recorded.

Sciatic Functional Index (SFI): SFI was determined from this formula.

$$SFI = -38.3 \times \frac{EPL - NPL}{NPL} + 109.5 \times \frac{ETS - NTS}{NTS} + 13.3$$

$$\times \frac{EIT - NIT}{NIT} - 8.8 \tag{2}$$

where *PL* indicates the footprint length, *TS* denotes the total toe spread, *IT* stands for intermediate toe spread, *E* is the injured side, and *N* represents the distance on the contralateral side.[61] **Scheme 2** represents the schematic diagram of the paw indicating *PL*, *TS*, and *IT* for a better understanding.

Tissue Collection: The animals were sacrificed after 6 weeks post-implantation via dislocation of the cervical vertebrae to harvest the tissues. The surgical site was opened up to isolate the scaffold-wrapped area of the resected sciatic nerve in each rat. After separation, the nerve conduits containing the regenerated neural tissues were fixed with 10% neutral-buffered formalin (NBF) at RT for 24 h. The fixed tissues were used for immunohistochemistry (IHC) and H&E staining. Gastrocnemius muscles of the operated left legs were collected for wet weight measurement and HE staining.

H&E and IHC Staining: Six weeks post-implantation, the regenerated nerves in the conduits were examined histologically. 5 μm thick

**ADVANCED
SCIENCE NEWS**

www.advancedsciencenews.com

**ADVANCED
HEALTHCARE
MATERIALS**

www.advhealthmat.de

longitudinal and cross sections were cut from the fixed samples using a microtome (Leica) and embedded in paraffin wax. The sections were deparaffinized with xylene and with a gradient of diluted ethanol (100%, 90%, 70%, and 50%). They were further rehydrated, which was followed by gentle rinsing in tap water and stained with freshly prepared HE.[62] The sections were dried and mounted on coverslips in DPX (di-styrene, a plasticizer, and xylene) (SRL, India). A microscope with RGB (Red, Green, Blue) filters (Lionheart LX, BioTek, USA) was used to image the stained sections to observe the morphology of regenerated nerve tissues.

Immunofluorescence was performed on cross-sections and longitudinal sections taken from the central portion of the regenerated tissues in the conduit after staining for NF200 and S-100. The procedure described above for IHC staining was used. After rehydration, antigen retrieval was carried out by incubating for 3 min under moist pressure in sodium citrate buffer (pH 6). After rinsing in Tris-buffered saline (pH 7.6), the sections were dried. 1% BSA was used for 2 h as a blocking agent, followed by overnight incubation with mouse monoclonal NF-160 (Sigma-Aldrich, USA) and rabbit polyclonal S100 (Invitrogen, USA) at 4 °C. The sections were washed with Tris-buffered saline containing 0.1% Tween® 20 Detergent (TBST) and incubated with rabbit anti-mouse IgG (H + L) − fluorescein isothiocyanate conjugate (Thermo, USA) secondary antibody for NF-160 and the goat antirabbit IgG (H + L) −tetramethylrhodamine isothiocyanate conjugate (Thermo, USA) secondary antibody for S100 for 2 h followed by washing with TBST. The sections were counterstained with DAPI (HiMedia). Finally, the samples were observed using an epi-fluorescence microscope (Lionheart LX, BioTek, USA). At least three areas were sampled for each section/group.

Statistical Analysis: The results are presented as mean ± standard error for each group. GraphPad Prism 5.04 was used for the statistical analysis (GraphPad Software, USA). One-way ANOVA was used for the statistical analysis, which was then followed by Dunnett and Tukey tests for significance. All analyses were carried out at a 95% confidence level and were considered to be significant at statistical probability $p < 0.05$. Statistical significances were denoted as (*/#/@), (**/##/@@) and (***/###/@@@) for $p < 0.05$, $p < 0.01$, and $p < 0.001$, respectively.

Supporting Information

Supporting Information is available from the Wiley Online Library or from the author.

Conflict of Interest

The authors have filed a patent application. No other conflicts to declare.

Data Availability Statement

The data that support the findings of this study are available from the corresponding author upon reasonable request.

[1] F. Momeni, X. Liu, J. Ni, *Mater. Des.* **2017**, *122*, 42.

[2] J. Choi, O.-C. Kwon, W. Jo, H. J. Lee, M.-W. Moon, *3D Print. Addit. Manuf.* **2015**, *2*, 159.

[3] Z. Ding, C. Yuan, X. Peng, T. Wang, H. J. Qi, M. L. Dunn, *Sci. Adv.* **2017**, *3*, 1602890.

[4] A. Subash, B. Kandasubramanian, *Eur. Polym. J.* **2020**, *134*, 109771.

[5] Y. S. Alshebly, M. Nafea, M. S. M. Ali, H. A. Almurib, *Eur. Polym. J.* **2021**, *159*, 110708.

[6] Y. Y. C. Choong, S. Maleksaeedi, H. Eng, S. Yu, J. Wei, P.-C. Su, *Appl. Mater. Today* **2020**, *18*, 100515.

[7] A. Sydney Gladman, E. A. Matsumoto, R. G. Nuzzo, L. Mahadevan, J. A. Lewis, *Nat. Mater.* **2016**, *15*, 413.

[8] J. Lai, X. Ye, J. Liu, C. Wang, J. Li, X. Wang, M. Ma, M. Wang, *Mater. Des.* **2021**, *205*, 109699.

[9] J. Zhang, Z. Yin, L. Ren, Q. Liu, L. Ren, X. Yang, X. Zhou, *Adv. Mater. Technol.* **2022**, *7*, 2101568.

[10] T. Mu, L. Liu, X. Lan, Y. Liu, J. Leng, *Compos. Sci. Technol.* **2018**, *160*, 169.

[11] H. Wei, Q. Zhang, Y. Yao, L. Liu, Y. Liu, J. Leng, *ACS Appl. Mater. Interfaces* **2017**, *9*, 876.

[12] Y. S. Lui, W. T. Sow, L. P. Tan, Y. Wu, Y. Lai, H. Li, *Acta Biomater.* **2019**, *92*, 19.

[13] P. Rastogi, B. Kandasubramanian, *Chem. Eng. J.* **2019**, *366*, 264.

[14] B. Narupai, P. T. Smith, A. Nelson, *Adv. Funct. Mater.* **2021**, *31*, 2011012.

[15] C. A. Spiegel, M. Hippler, A. Münchinger, M. Bastmeyer, C. Barner-Kowollik, M. Wegener, E. Blasco, *Adv. Funct. Mater.* **2020**, *30*, 1907615.

[16] F. Zhang, L. Wang, Z. Zheng, Y. Liu, J. Leng, *Composites, Part A* **2019**, *125*, 105571.

[17] J. del Barrio, C. Sánchez-Somolinos, *Adv. Opt. Mater.* **2019**, *7*, 1900598.

[18] F. M. Yavitt, B. E. Kirkpatrick, M. R. Blatchley, K. S. Anseth, *ACS Biomater. Sci. Eng.* **2022**, *8*, 4634.

[19] K. Zhang, A. Geissler, M. Standhardt, S. Mehlhase, M. Gallei, L. Chen, C. Marie Thiele, *Sci. Rep.* **2015**, *5*, 11011.

[20] H. Chathuranga, I. Marriam, Z. Zhang, J. MacLeod, Y. Liu, H. Yang, C. Yan, *Adv. Mater. Technol.* **2022**, *7*, 2100447.

[21] H. Wu, O. Wang, Y. Tian, M. Wang, B. Su, C. Yan, K. Zhou, Y. Shi, *ACS Appl. Mater. Interfaces* **2020**, *13*, 12679.

[22] X. Wan, X. He, Y. Liu, J. Leng, *Addit. Manuf.* **2022**, *53*, 102689.

[23] S. H. Kim, Y. B. Seo, Y. K. Yeon, Y. J. Lee, H. S. Park, M. T. Sultan, J. M. Lee, J. S. Lee, O. J. Lee, H. Hong, *Biomaterials* **2020**, *260*, 120281.

[24] C. Cui, D.-O. Kim, M. Y. Pack, B. Han, L. Han, Y. Sun, L.-H. Han, *Biofabrication* **2020**, *12*, 045018.

[25] P. Dorishetty, N. K. Dutta, N. R. Choudhury, *Adv. Colloid Interface Sci.* **2020**, *281*, 102163.

[26] H. Zhao, M. Liu, Y. Zhang, J. Yin, R. Pei, *Nanoscale* **2020**, *12*, 14976.

[27] T. Distler, A. R. Boccaccini, *Acta Biomater.* **2020**, *101*, 1.

[28] M. C. Mulakkal, R. S. Trask, V. P. Ting, A. M. Seddon, *Mater. Des.* **2018**, *160*, 108.

[29] L. Zhang, Y. Xiang, H. Zhang, L. Cheng, X. Mao, N. An, L. Zhang, J. Zhou, L. Deng, Y. Zhang, *Adv. Sci.* **2020**, *7*, 1903553.

[30] A. Zolfagharian, A. Kaynak, S. Y. Khoo, A. Kouzani, *Sens. Actuators, A* **2018**, *274*, 231.

[31] Y. Chen, J. Zhang, X. Liu, S. Wang, J. Tao, Y. Huang, W. Wu, Y. Li, K. Zhou, X. Wei, *Sci. Adv.* **2020**, *6*, aba7406.

[32] H. Cheong, Y.-J. Jun, E. Y. Jeon, J. I. Lee, H. J. Jo, H. Y. Park, E. Kim, J. W. Rhie, K. I. Joo, H. J. Cha, *Chem. Eng. J.* **2022**, *445*, 136641.

[33] A. Kirillova, R. Maxson, G. Stoychev, C. T. Gomillion, L. Ionov, *Adv. Mater.* **2017**, *29*, 1703443.

[34] A. Ding, O. Jeon, D. Cleveland, K. L. Gasvoda, D. Wells, S. J. Lee, E. Alsberg, *Adv. Mater.* **2022**, *34*, 2109394.

[35] I. Apsite, G. Constante, M. Dulle, L. Vogt, A. Caspari, A. R. Boccaccini, A. Synytska, S. Salehi, L. Ionov, *Biofabrication* **2020**, *12*, 035027.

[36] J. Uribe-Gomez, A. Posada-Murcia, A. Shukla, M. Ergin, G. Constante, I. Apsite, D. Martin, M. Schwarzer, A. Caspari, A. Synytska, *ACS Appl. Bio Mater.* **2021**, *4*, 1720.

[37] G. Constante, I. Apsite, H. Alkhamis, M. Dulle, M. Schwarzer, A. Caspari, A. Synytska, S. Salehi, L. Ionov, *ACS Appl. Mater. Interfaces* **2021**, *13*, 12767.

[38] A. Urciuolo, I. Poli, L. Brandolino, P. Raffa, V. Scattolini, C. Laterza, G. G. Giobbe, E. Zambaiti, G. Selmin, M. Magnussen, *Nat. Biomed. Eng.* **2020**, *4*, 901.

[39] J. Wang, H. Xiong, T. Zhu, Y. Liu, H. Pan, C. Fan, X. Zhao, W. W. Lu, *ACS Nano* **2020**, *14*, 12579.

[40] D. Petta, D. W. Grijpma, M. Alini, D. Eglin, M. D'Este, *ACS Biomater. Sci. Eng.* **2018**, *4*, 3088.

[41] M. Shin, J. H. Galarraga, M. Y. Kwon, H. Lee, J. A. Burdick, *Acta Biomater.* **2019**, *95*, 165.

[42] Y. P. Singh, A. Bandyopadhyay, B. B. Mandal, *ACS Appl. Mater. Interfaces* **2019**, *11*, 33684.

[43] A. Bandyopadhyay, B. B. Mandal, N. Bhardwaj, *J. Biomed. Mater. Res., Part A* **2022**, *110*, 884.

[44] A. Singh, S. Asikainen, A. K. Teotia, P. A. Shiekh, E. Huotilainen, I. Qayoom, J. Partanen, J. Seppälä, A. Kumar, *ACS Appl. Mater. Interfaces* **2018**, *10*, 43327.

[45] M. R. MacEwan, E. R. Zellmer, J. J. Wheeler, H. Burton, D. W. Moran, *Front. Neurosci.* **2016**, *10*, 557.

[46] A. Pabari, S. Y. Yang, A. M. Seifalian, A. Mosahebi, *J. Plast., Reconstr. Aesthetic Surg.* **2010**, *63*, 1941.

[47] R. Li, Y. Li, Y. Wu, Y. Zhao, H. Chen, Y. Yuan, K. Xu, H. Zhang, Y. Lu, J. Wang, *Biomaterials* **2018**, *168*, 24.

[48] V. C. Anseloni, M. Ennis, M. S. Lidow, *J. Neurosci. Methods* **2003**, *131*, 93.

[49] A.-L. Cattin, J. J. Burden, L. Van Emmenis, F. E. Mackenzie, J. J. Hoving, N. G. Calavia, Y. Guo, M. McLaughlin, L. H. Rosenberg, V. Quereda, *Cell* **2015**, *162*, 1127.

[50] B. Zhao, Z. Zhao, J. Ma, X. Ma, *Neurosci. Lett.* **2019**, *705*, 259.

[51] R. K. Jain, P. Au, J. Tam, D. G. Duda, D. Fukumura, *Nat. Biotechnol.* **2005**, *23*, 821.

[52] C. Chen, J. Tang, Y. Gu, L. Liu, X. Liu, L. Deng, C. Martins, B. Sarmento, W. Cui, L. Chen, *Adv. Funct. Mater.* **2019**, *29*, 1806899.

[53] A. D. Gaudet, P. G. Popovich, M. S. Ramer, *J. Neuroinflammation* **2011**, *8*, 110.

[54] Y. Zhao, Q. Zhang, L. Zhao, L. Gan, L. Yi, Y. Zhao, J. Xue, L. Luo, Q. Du, R. Geng, *ACS Omega* **2017**, *2*, 7471.

[55] L. Yao, G. C. de Ruiter, H. Wang, A. M. Knight, R. J. Spinner, M. J. Yaszemski, A. J. Windebank, A. Pandit, *Biomaterials* **2010**, *31*, 5789.

[56] A. Faroni, S. A. Mobasseri, P. J. Kingham, A. J. Reid, *Adv. Drug Delivery Rev.* **2015**, *82*, 160.

[57] W. Ye, H. Li, K. Yu, C. Xie, P. Wang, Y. Zheng, P. Zhang, J. Xiu, Y. Yang, F. Zhang, *Mater. Des.* **2020**, *192*, 108757.

[58] W. Zhu, K. R. Tringale, S. A. Woller, S. You, S. Johnson, H. Shen, J. Schimelman, M. Whitney, J. Steinauer, W. Xu, *Mater. Today* **2018**, *21*, 951.

[59] D. Podstawczyk, M. Nizioł, P. Szymczyk, P. Wiśniewski, A. Guiseppi-Elie, *Addit. Manuf.* **2020**, *34*, 101275.

[60] T. Dowdall, I. Robinson, T. F. Meert, *Pharmacol., Biochem. Behav.* **2005**, *80*, 93.

[61] J. Bain, S. Mackinnon, D. Hunter, *Plast. Reconstr. Surg.* **1989**, *83*, 129.

[62] S. Ghosh, S. Haldar, S. Gupta, A. Bisht, S. Chauhan, V. Kumar, P. Roy, D. Lahiri, *ACS Appl. Bio Mater.* **2020**, *3*, 5796.